AIP | Review of Scientific Instruments

Low noise Kα-band hopping reflectometer based on yttrium iron garnet sources at TEXTOR

S. Soldatov, A. Krämer-Flecken, and O. Zorenko

Citation: Rev. Sci. Instrum. **82**, 033513 (2011); doi: 10.1063/1.3567779
View online: http://dx.doi.org/10.1063/1.3567779
View Table of Contents: http://rsi.aip.org/resource/1/RSINAK/v82/i3
Published by the American Institute of Physics.

Low noise K_α-band hopping reflectometer based on yttrium iron garnet sources at TEXTOR

S. Soldatov,[1,a)] A. Krämer-Flecken,[1] and O. Zorenko[2]
[1]*Institute of Energy and Climate Research — Plasma Physics, Forschungszentrum Jülich GmbH, Association EURATOM–FZJ, Partner In the Trilateral Euregio Cluster, Jülich, Germany*
[2]*State Research Institute "ORION," 03680 Kyiv, Ukraine*

(Received 14 December 2010; accepted 12 February 2011; published online 31 March 2011)

The heterodyne hopping reflectometer system based on wide-tuned low noise yttrium iron garnet sources was developed for TEXTOR experiment. Being installed in 1998 it successfully operates more than 10 years providing the measurements of plasma density fluctuations. Owing to the advance multihorn antennae systems installed at three different positions around the tokamak, the correlation properties as well as the propagation measurements of plasma density fluctuations are realized. The reflectometer operates in ordinary polarization mode providing the access mostly to plasma gradient and pedestal region. The capabilities of the diagnostic are illustrated with the examples of measured fluctuation characteristics in the variety of TEXTOR plasmas. © *2011 American Institute of Physics*. [doi:10.1063/1.3567779]

I. INTRODUCTION

Reflectometry is widely used as a diagnostic in fusion plasmas. Its advantages are neutron robustness, the possibility of conveying microwaves to a remote location, and the relative simplicity of installation inside the vacuum vessel. Historically radial correlation reflectometers are more widely distributed,[1–6] as compared to poloidal/toroidal correlation reflectometers,[7–10] which have the probing areas on the same reflecting surface allocated. The latter approach presumes the usage of several receiving antennas with corresponding waveguide lines, additional detectors, and electronics modules that usually results in more complicated and expensive solutions as compared with radial correlation ones.

On the Toroidal EXperiment for Technical Oriented Research (TEXTOR) the heterodyne hopping reflectometer system based on the pair of wide-tuned yttrium iron garnet (YIG) sources was developed. Being installed in 1998 it successfully operates more than 10 years providing the measurements of both spectral and correlation properties of plasma density fluctuations. Among them are the propagation velocity, the correlation length, and decorrelation time. The YIG-based reflectometer constitutes an integrated reflectometry system, which includes one more reflectometer for the same K_α frequency band installed in 2008.[11] This paper describes the YIG-based reflectometer hardware and to some extent the correlation approach used in multiantennae registration.

The paper is organized as follows. The system design and principles are presented in Sec. II. In Sec. III the waveguide and intermediate frequency (IF) circuitry are described. The multihorn antenna system and the details of the approach used for correlation measurements, are presented in Sec. IV. The system performance and capabilities are presented in Secs. V and VI, respectively. The results are concluded in Sec. VII.

II. DESIGN AND OPERATIONAL PRINCIPLES

The simplified block-scheme of reflectometer is presented in Fig. 1. The transmitted signals are generated by two identical separate YIG-tuned oscillators. A YIG-tuned oscillator is a solid-state oscillator whose tunable element is a sphere of yttrium iron garnet. Gallium is added to dope the sphere to extend the frequency range. These materials have extremely high unloaded q-factors whose resonant frequency is varied by an externally applied magnetic field. A single sphere, properly coupled to a microwave circuit, is used for frequency tuning. Specially developed YIG sources can be tuned over full K_α band 26.0–37.0 GHz having an output power of more than 13 dBm with the flatness of $\sim$3 dBm. The absence of frequency multipliers and power amplifiers in the scheme is an essential advantage allowing to minimize the system noise figure.

Two YIG sources are locked with a constant 20 MHz frequency difference (or IF) using a phase locked loop (PLL) circuit. Digital-to-analog convertors (DAC1 and DAC2) provide the control voltage for sources YIG1 and YIG2, respectively. The rf power from every source is decoupled using a 10 dB directional couplers (DC1, DC2) and isolators (ISL2, ISL3) for subsequent frequency down converting with the mixer (Mix) to IF. This reference IF signal is amplified by a broadband limiting amplifier (Amp3 + Lim1) in a such way that its minima and maxima match the voltage intervals corresponding to logic "0" and "1," respectively. After that, it is supplied to the first arm of the digital PLL. On the second arm the signal from a crystal 20 MHz oscillator (Osc1) is supplied. The PLL compares the signals in both arms and generates the output corrective signal which is supplied (after amplification in Amp2 and filtering out with proportional-integrated filter PIF) to the circuit controlling the current in additional (fast) winding of YIG2.

The microcontroller (MC) governs the frequency of both sources in time by means of DAC1 and DAC2, analyzing the logic signals coming from PLL and from the calibrating

[a)] Also at Department of Applied Physics, Ghent University, 9000 Gent, Belgium. Electronic mail: s.soldatov@fz-juelich.de.

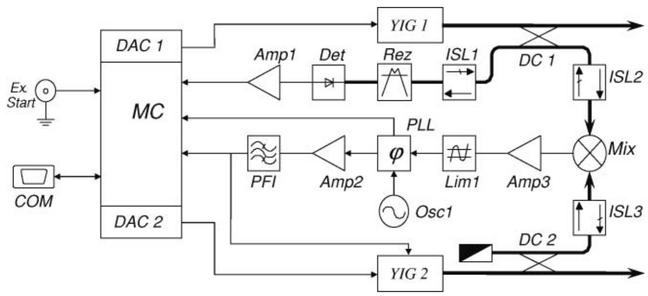

FIG. 1. Simplified block diagram of the hopping K_α-band reflectometer. The waveguide structures are outlined by thick lines.

circuit resonant at 26 GHz. The latter one is used for automatic self-calibrating procedure. In spite of high linearity of YIG sources they always have the thermal drift (tenth of MHz). While the thermal conditions are not stationary during an experiment, the frequency of the sources is the function of time. To avoid sizeable instrumental errors the procedure of the frequency calibration is fulfilled after every preprogramming of the MC or every measurement cycle.

A. Self-calibration procedure

The calibrating circuit consists of the passive high-quality 26 GHz resonator (Rez), microwave detector (Det), and amplifier (Amp1), see Fig. 1. The rf power from YIG1 is supplied to the calibrating arm with the use of directional coupler (DC1) and isolator (ISL1). In Fig. 2 the logical control during the self-calibration procedure (stages I–IV) and the hopping operation (stage V) are illustrated. The calibration starts with the setting of DAC1 and DAC2 to the lowest level corresponding to the frequency of 25.75 GHz. Next, MC increases the control voltage on YIG1 until the frequency becomes equal to 26 GHz and logic signal from resonator is generated. As soon as the resonator logic signal is available at MC the voltage scan is stopped and the current voltage value is stored in the memory of MC. After that, the MC starts to drive the DAC2 to increase the frequency on YIG2 until it will be locked by PLL with YIG1 at the frequency 26 GHz + IF, where IF = 20 MHz. Next, the MC increases the frequency of both sources equally up to the first frequency in the sequence preprogrammed by operator. The calibration is finished, and the system waits for the external start pulse (Ext. Start) to perform the frequency scan according to the task.

B. Computer interface program

The microcontroller can be preprogrammed either using the keyboard on the right side of the device or through a COM port connected to the remote personal computer with the use of interface program. The latter possibility is normally realized during the plasma experiment when the reflectometer is managed by an operator in TEXTOR control room. The window of interface program is shown in Fig. 3 (left). On the left upper subwindow, the status of system as whole as well as the logical signals of 26 GHz resonator, PLL, external start, receiving, and transmitting ability through the COM port are shown. Furthermore, the duration of a single frequency step (t_s) is displayed. On the lower left subwindow "Settings," an operator can input the frequency sequence $f_1, f_2, \ldots, f_N$, $1 < N < 20$ as well as the total time of measurements ($0.13 < T < 10$ s), COM port number, and an increment of the controlling voltage (sweep speed) within $1 < V_u < 5$ V/s. The durations of steps ($t_{s1} = t_{s2} = \cdots = t_{sN} = t_s$) are equally distributed within $0 < t < T$ by MC, however $t_s \cdot N < T$ because the system needs some time for tuning between steps. To upload/download the input settings to/from the MC's memory as well as to emulate the external start pulse three buttons in the bottom are used. The right subwindow is an in situ monitor for DAC1, DAC2, and PLL voltages as well as for the logical signals of 26 GHz

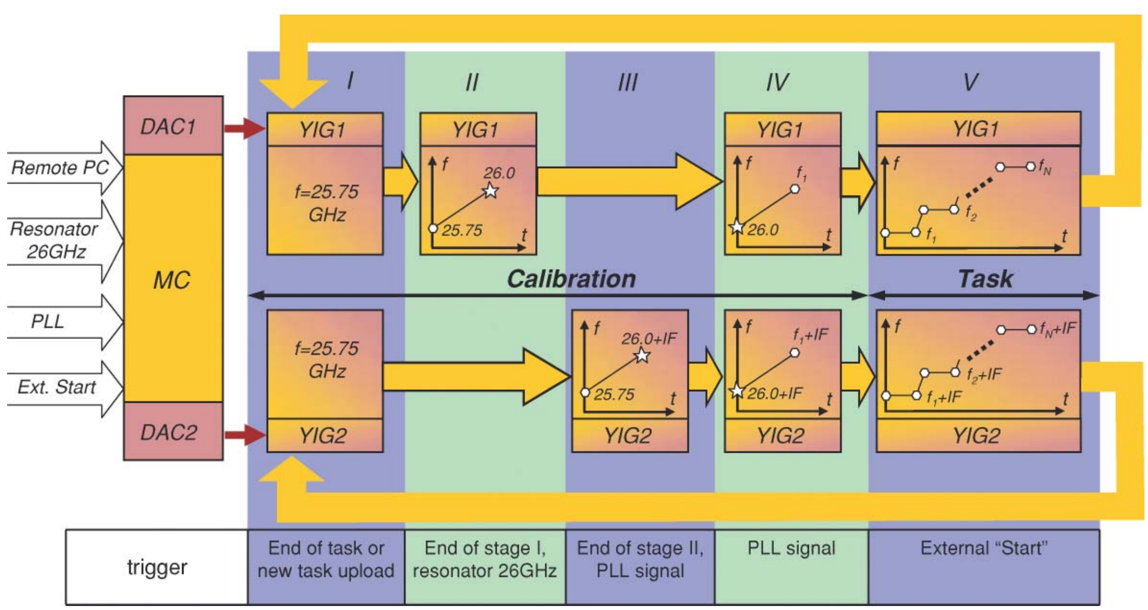

FIG. 2. (Color online) Block diagram illustrating the logical control of YIG sources by the internal microcontroller (MC) during a measurement cycle I → V. Stages I to IV consist of the self-calibration procedure. Stage V is the hopping operation ($f_1, f_2, \ldots, f_n$) according to the preprogrammed task.

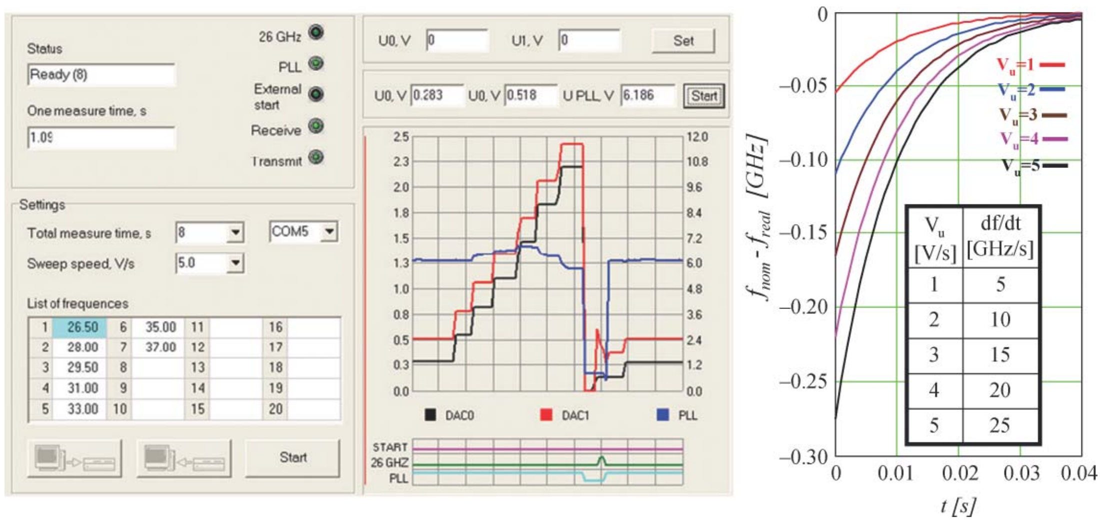

FIG. 3. (Color online) (left) The window of interface program during plasma discharge. (right) A postdrift effect for different sweep speed, V_u. The real frequency, f_{real}, approaches the preprogrammed one, f_{nom}, after the end of tuning phase ($t = 0$).

resonator, PLL, and external start. Here, the snapshot for seven frequency steps is shown as an example where the stepwise traces of controlled voltages are visible.

Note that in spite of sources are phase locked during the sweep between steps, this period is not used for the measurements. Due to a transient process in the YIG sources there is a postdrift effect and the real frequency f_{real} is not equal to the nominal frequency f_{nom}, where f_{nom} is one from the preprogrammed sequence $f_1, f_2, \ldots, f_N$. When the system reports that it operates at the frequency f_{nom}, in fact $f_{\text{real}} < f_{\text{nom}}$. The difference $f_{\text{nom}} - f_{\text{real}}$ reduces in time and f_{real} approaches f_{nom}. These dependencies for different V_u are presented in Fig. 3 (right).

III. WAVEGUIDE SYSTEM AND IF CIRCUITRY

The hopping reflectometer is placed in a cabinet ~3 m away from TEXTOR. The microwaves from reflectometer to antenna system and back are conveyed by the standard WR28 rectangular copper waveguides operating in TE_{01} fundamental mode. Waveguides pass the upper port of tokamak where a vacuum window made by a Kapton sheet with a thickness of 0.8 mm is installed. The window also serves as an electric insulation of reflectometer from the tokamak vacuum vessel. Three 3 dB directional couplers are used to branch the heterodyne power to four receiving channels (Fig. 4). Every channel contains the balanced mixer where the probing microwaves reflected from fluctuating plasma are mixed with the heterodyne microwave radiation and down converted to $\widetilde{\text{IF}}$ (a tilde means the modulation by plasma). The ferrite isolators are settled from both sides of every mixer to prevent (i) the radiation of the heterodyne power to the plasma and (ii) the leakage of the reflected power between the channels. The intermediate frequency ($\widetilde{\text{IF}}$) signals at the output of the mixers are amplified and bandpass filtered in the band 20 ± 2 MHz and transmitted to the first input of the I/Q detector. The second input of the I/Q detector is fed by the reference IF signal outgoing from the balanced mixer in the reflectometer shown in Fig. 1. The output signals $A \cdot \cos(\varphi)$ and $A \cdot \sin(\varphi)$ are acquired by analog-to-digital convertor, ADC, with a frequency < 3 MHz and stored to TEXTOR data base.

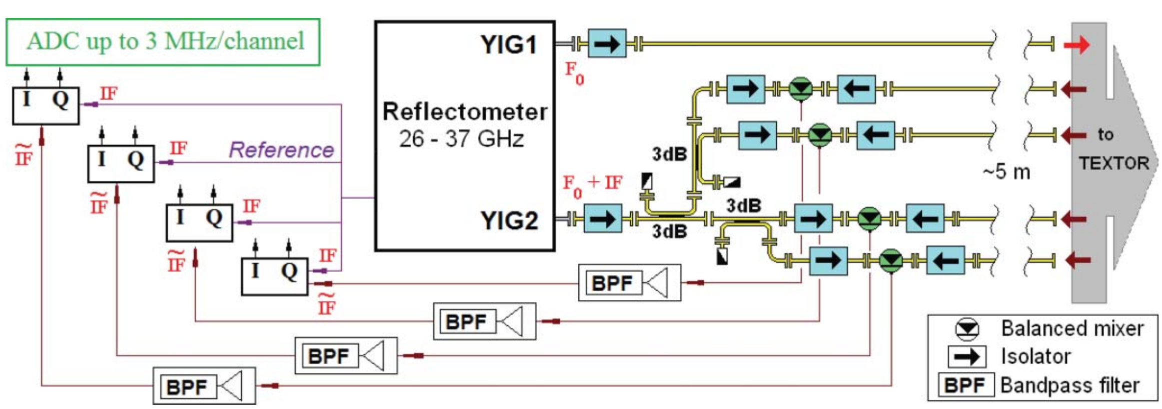

FIG. 4. (Color online) The waveguide and IF circuitry of the reflectometery system.

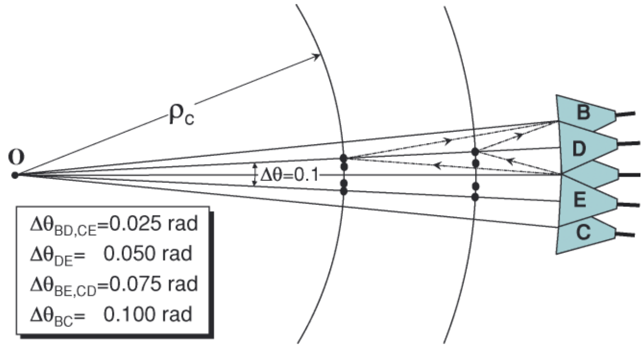

FIG. 5. (Color online) The LFS antenna system layout (horns are not on the scale!). The middle horn is a launcher and others (B, C, D, E) are receivers. The reflecting areas are shown as black spots for two density surfaces as an example. Owing to the antennas are aimed to the center of vacuum vessel "**O**" the poloidal distances between reflecting areas are approximately the same for different ρ_c.

IV. ANTENNAE SYSTEM

A. Design

The antenna system is installed inside the vacuum vessel at a distance of 56 cm from its center and at ~10 cm away from the last closed flux surface, at the low field side (LFS) of the tokamak (poloidal angle $\theta = 0°$). The system consists of the five equivalent pyramidal horns with a focal length of 8.0 cm. The antenna mouth is rectangular, its external and internal dimensions are 4.9 × 3.2 and 4.6 × 2.9 cm, respectively. The width of the radiation pattern in the poloidal direction amounts to 0.28 rad for vacuum propagation.[12] Two-dimensional full-wave modeling have shown that the sensitivity to fluctuation perpendicular wave number $k_\perp$ for TEXTOR geometry is maximal at $k_\perp = 0$ and decreases toward $k_\perp \approx 4\,\text{cm}^{-1}$ by ~10 times.[12] The deterioration toward higher $k_\perp$ does not affect neither correlation nor time delay measurements. All five antennas are aimed to the center of the vacuum vessel, see Fig. 5, and combined in two adjacent columns. One column consists of three horns and another one is of two horns. Though the horns are distributed both poloidally and toroidally, the system is symmetrical relative to the plane of symmetry of the middle horn, see Figs. 5 and 6. The middle horn is used as a launcher and the four others (marked as "B," "C," "D," and "E") as receivers. Such a scheme provides four adjacent probing areas lying on the same density surface $n_e(\rho) = n_c$ and spaced poloidally by

$$\begin{aligned} \widehat{BD}_\theta &= \widehat{CE}_\theta = 0.025\,\text{rad}, \quad \widehat{DE}_\theta = 0.05\,\text{rad}, \\ \widehat{BE}_\theta &= \widehat{CD}_\theta = 0.075\,\text{rad}, \quad \widehat{BC}_\theta = 0.1\,\text{rad}. \end{aligned} \tag{1}$$

In 2007 a similar five-horn antenna system was installed on the top of the tokamak in the neighboring toroidal cross section ($\Delta\varphi = 22.5°$ apart from the equatorial system). And the equatorial system was replaced by the analogous one but consisting of the cone antennas. In 2009 a new antenna system of three pyramidal quadratic horns (one launcher plus two receivers) was installed additionally at equatorial LFS position for long-range correlation measurements toroidally 90° and 112.5° apart from the equatorial and top systems, respectively.[11] Thus, presently correlation reflectometry (CR) operates with three antenna systems installed around the tokamak.

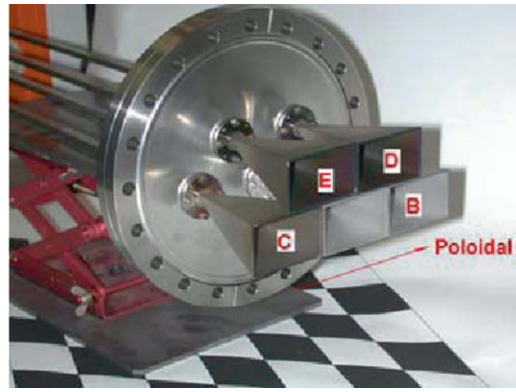

FIG. 6. (Color online) A photo of the LFS antenna system.

B. Correlation approach

Owing to the antennae system is symmetrical and focused to the center of the vacuum vessel, from one hand side, and nested, concentric geometry of the cutoff surfaces ($\rho = \rho_c$), from another hand side, the poloidal separations [Eq. (1)] between probing areas are nearly constant for $0.5 \lesssim \rho_c/a \lesssim 1$ radial range, see Fig. 5. For inner part of plasma column the Shafranov shift of flux surfaces becomes sufficient and corrections for distances between reflecting areas are required. If the density fluctuations propagate across the antennae system (due to a plasma rotation and/or drifts) and the fluctuations lifetime is long enough as compared with its propagation time the *correlation method* allows to measure the propagation velocity. The *correlation method* presumes the analysis either in time domain (a shift of maximum of the cross-correlation function) or in frequency domain (a derivative of the cross-phase). Combining four receiving channels in six pairs *BC*, *BD*, *BE*, *CD*, *CE*, *DE* we measure the sequence of time delays, Δt,

$$\Delta t = \{\Delta t_{BC}, \Delta t_{BD}, \Delta t_{BE}, \Delta t_{CD}, \Delta t_{CE}, \Delta t_{DE}\}.$$

By definition, if Δx is a linear distance along the velocity of propagation $\vec{\upsilon}$ and ρ is the radius of propagation path then

$$\Delta t = \frac{\Delta x}{|\vec{\upsilon}|} = \frac{\Delta\zeta}{\Omega}, \tag{2}$$

where $\Omega = \upsilon/\langle\rho\rangle$ and $\Delta\zeta = \Delta x/\langle\rho\rangle$ are the angular velocity and angular distance, respectively. We presume also $|\vec{\upsilon}| = \text{const}$ during a propagation time and $\langle\rho\rangle$ is a mean radius of the curvature of the propagation path.

Since the density fluctuations are highly elongated along the magnetic field lines ($\vec{B}$), the diagnostic measures the time delay due to the velocity component perpendicular to the magnetic field only (a parallel component is degenerated): $\upsilon = \vec{\upsilon}^{\text{turb}} \times \vec{B}/B = \upsilon^{\text{turb}}_{\perp_B}$. Due to such geometry, the velocity component parallel to $\vec{B}$ cannot be measured with present method and Eq. (2) has to be rewritten as

$$\Delta t_{\text{refl}} = \frac{\Delta\zeta_\perp}{\Omega_\perp}, \tag{3}$$

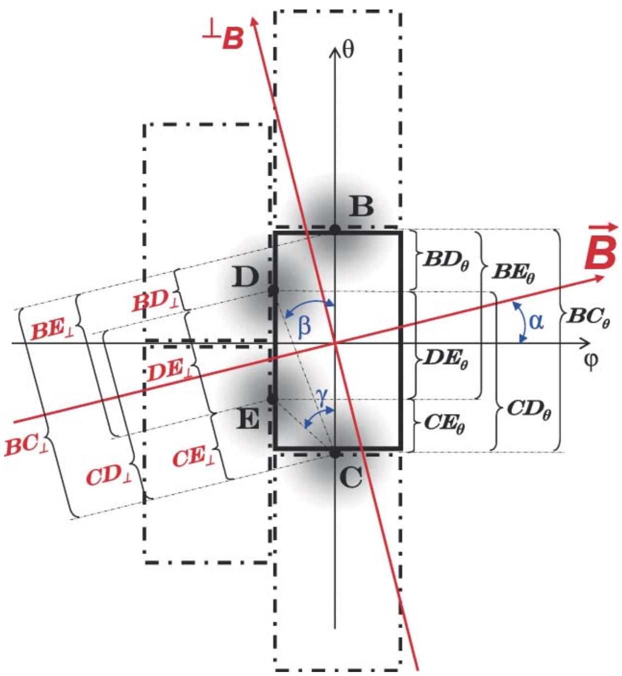

FIG. 7. (Color online) A sketch of antennas front ends shown by rectangles and reflecting areas corresponding to receiving horns B, C, D, E shown by gray-scaled circular spots. α is a pitch angle of the magnetic field; β and γ are geometrical factors.

where $\Delta\zeta_\perp$ is the projection of angular distance defined in Eq. (1) to $\perp_B$ direction (see Fig. 7),

$$\widehat{BD}_\perp = \frac{\widehat{BD}_\theta}{\cos(\gamma)}\cdot\cos(\gamma+\alpha),\quad \widehat{CE}_\perp = \frac{\widehat{CE}_\theta}{\cos(\gamma)}\cdot\cos(\gamma-\alpha),$$
$$\widehat{BE}_\perp = \frac{\widehat{BE}_\theta}{\cos(\beta)}\cdot\cos(\beta+\alpha),\quad \widehat{CD}_\perp = \frac{\widehat{CD}_\theta}{\cos(\beta)}\cdot\cos(\beta-\alpha),$$
$$\widehat{DE}_\perp = \widehat{DE}_\theta\cdot\cos(\alpha),\quad \widehat{BC}_\perp = \widehat{BC}_\theta\cdot\cos(\alpha). \tag{4}$$

Here α is a pitch angle of the magnetic field and β and γ are the angles defined by the antennas geometry. The velocity and correlation measurements based on Eqs. (3) and (4) are not trivial because they require the knowledge of the dependencies $\beta(\rho_c)$ and $\gamma(\rho_c)$ as well as the ρ_c itself. Note that the system of equations (4) can provide the information about the pitch angle α if at least three of four receiving signals are measured.[11]

To increase the validity of the measurements, to reduce the errors, and to automate the data processing on the most effective way we utilize the following procedure. Using the symmetry in above equations it is possible to average out the contribution of the geometrical factors β and γ in cross-pairs $\widehat{BD}_\perp$ and $\widehat{CE}_\perp$ as well as in $\widehat{BE}_\perp$ and $\widehat{CD}_\perp$ employing Eqs. (1) and (4) as follows:

$$\begin{aligned}\Delta\zeta_{\perp 1} &= 0.5\cdot(\widehat{BD}_\perp+\widehat{CE}_\perp)\\ &= 0.5\cdot(\widehat{BD}_\theta+\widehat{CE}_\theta)\cdot\cos(\alpha)\approx 0.025\,\text{rad},\\ \Delta\zeta_{\perp 3} &= 0.5\cdot(\widehat{BE}_\perp+\widehat{CD}_\perp)\\ &= 0.5\cdot(\widehat{BE}_\theta+\widehat{CD}_\theta)\cdot\cos(\alpha)\approx 0.075\,\text{rad},\end{aligned} \tag{5}$$

where $\Delta\zeta_{\perp 1}$ and $\Delta\zeta_{\perp 3}$ are averaged perpendicular distances for $\widehat{BD}_\perp$, $\widehat{CE}_\perp$ and $\widehat{BE}_\perp$, $\widehat{CD}_\perp$ pairs, respectively. For TEXTOR plasmas the pitch angle is of $\lesssim 0.1$ rad therefore we take the approximation $\cos(\alpha)\approx 1$ and found $\Delta\zeta_{\perp 1}$ and $\Delta\zeta_{\perp 3}$ are approximately equal to the distances defined in Eq. (1). The time delays corresponding to these propagation paths [based on Eq. (3)] are also simple averages,

$$\begin{aligned}\Delta t_1 &= 0.5\cdot(\Delta t_{BD}+\Delta t_{EC}),\\ \Delta t_3 &= 0.5\cdot(\Delta t_{BE}+\Delta t_{CD}).\end{aligned} \tag{6}$$

Two other distances

$$\begin{aligned}\Delta\zeta_{\perp 2} &= \widehat{DE}_\perp = \widehat{DE}\cdot\cos(\alpha)\approx 0.05\,\text{rad},\\ \Delta\zeta_{\perp 4} &= \widehat{BC}_\perp = \widehat{BC}\cdot\cos(\alpha)\approx 0.1\,\text{rad}\end{aligned} \tag{7}$$

correspond to

$$\Delta t_2 = \Delta t_{DE},\quad \Delta t_4 = \Delta t_{BC}. \tag{8}$$

Thus, having four angular distances and four corresponding time delays defined in Eqs. (5)–(8) we calculate the propagation velocity as an average,

$$\Omega_\perp^{\text{turb}} = \Omega_{\text{refl}} = \frac{1}{4}\sum_{i=1}^{4}\frac{\Delta\zeta_{\perp_i}}{\Delta t_i}. \tag{9}$$

Alternatively, assuming the coefficient proportionality between Δt and $\Delta\zeta_\perp$ for all propagation distances equals to $1/\Omega_\perp^{\text{turb}}$, the method of linear regression can be employed to find the averaged velocity.[11] The measurements of the propagation velocity at four different distances increases the validity and robustness of the method and reduces the errors. The typical velocity error bars for ohmic heated plasmas are below 5% and for L-mode plasmas when the fluctuations lifetime is reduced the error bars increase to 5%–15%. We like to underline once again that for circular outermost TEXTOR plasmas and O-mode wave polarization the estimation of $\Omega_\perp^{\text{turb}}$ does not require the knowledge of the cutoff position since $\Delta\zeta_{\perp 1,2,3,4}$ are constant for any ρ_c.

V. SYSTEM PERFORMANCE

The performance of the system is defined mostly by the high linearity and low noise of YIG sources and well developed PLL system. The mean level of background noise is less than −60 dBm, see Fig. 8 (left), where the spectrum analyzer measurements in the lab are presented. In Fig. 8 (right) the detailed (200 Hz span) spectrum of IF is presented. The FWHM of IF line is ∼1 Hz, and the level of parasitic peaks (mostly due to mains supply) is less than −45 dBc.

The system performance as a whole can be estimated analyzing the spectra of the signals in plasma experiment. Figure 9 represents the power spectrum of the complex reflectometer signal measured in ohmic heated plasma. It illustrates a high dynamic range exceeding 60 dB which is achieved in the system.

An example of the reflectometer hopping operation during an ohmic heated plasma discharge is presented in Fig. 10. Nine frequency steps were preprogrammed: 26.0, 26.0, 26.0, 27.5, 31.0, 33.0, 35.0, 37.0, and 37.0 GHz. The whole interval of operation is of 4.5 s and the duration of a single step is of ≈0.45 s. The Fourier spectrogram of the

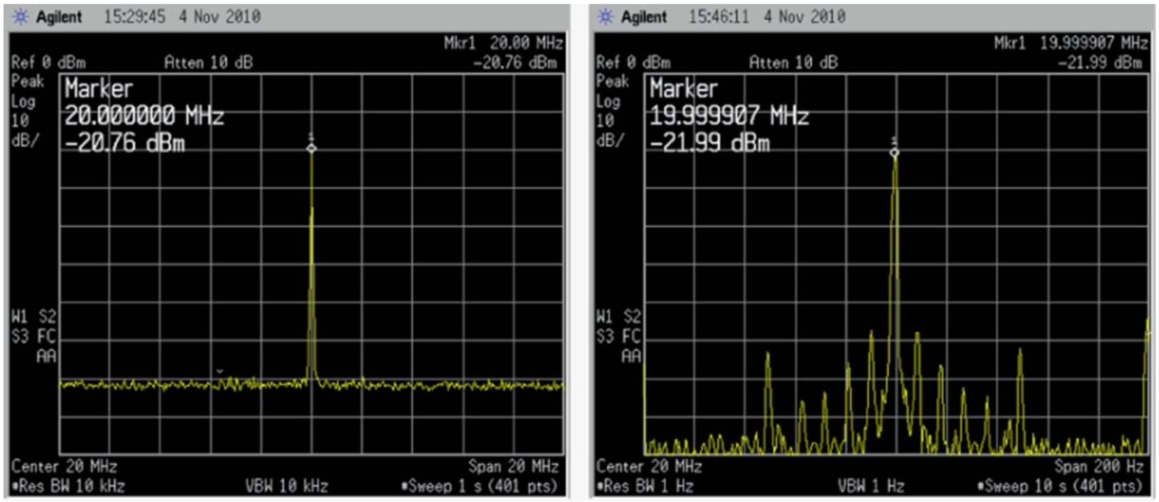

FIG. 8. (Color online) (left) Spectrum of IF measured at 20 MHz span. Mean level of background noise is less than −60 dBm. (right) Detailed spectrum of IF at 200 Hz span and 1 Hz video-band width. The peak-width at 3 dB level is ∼1 Hz. The level of parasitic harmonics is less than −45 dBc.

reflectometer signal, the cutoff radius (ρ_c) with line averaged density and plasma current as well as the operation frequency status "Fixed"/"Tuned" versus time are shown in Figs. 10(a), 10(b) and 10(c), respectively.

VI. DEMONSTRATION OF THE CAPABILITY

A. Spectral amplitude, cross-phase, and coherence

An example of the analysis of the reflectometry data in the frequency domain is represented in Fig. 11. Here two plasmas are compared: (i) with balanced neutral beam injection (NBI) heating of 0.8 MW and radius $\rho_c/a = 0.5$ (in the left coloumn) and (ii) with counter–I_p NBI of 1.3 MW and $\rho_c/a = 0.85$ (in the right coloumn). (TEXTOR is equipped with two tangential oppositely directed neutral beam injectors each with 1.5 MW of maximum power which can drive the plasma rotation.) The two upper graphs show the amplitude spectra for antennas B, C, D, and E. In the case of lower NBI power (0.8 MW) the turbulence level is smaller, and the fluctuations are more structured revealing the quasicoherent (QC) feature[13] in the spectrum centered at ≈40 kHz. The spectra in right column (NBI power of 1.3 MW) reveal a broadband feature of higher amplitude than that in the left graph. It results mostly from the higher turbulence level because of higher auxiliary heating power and increased ρ_c. Note that due to strong unbalanced NBI the higher plasma rotation leads to higher Doppler broadening of the spectra.

Six cross-phase spectra for six antennae combinations *BC*, *BD*, *BE*, *CD*, *CE*, *DE* are shown in Fig. 11(b). If fluctuations evolve slowly compared to the propagation time the cross-phase is a linear function of the frequency, and its derivation (or slope) is proportional to the propagation time between two reflecting areas (Δt). According to Eq. (4) the distances between reflecting areas are different, therefore the slopes in the corresponding cross-phase spectra are also different: the largest one corresponds to the largest distance $BC_\perp$ and the smallest one to the shortest $CE_\perp$. Furthermore, in the case of nonbalanced NBI (right graph) the plasma rotation is higher as compared to the case with balanced NBI (left graph). This agrees well with the smaller cross-phase slopes in the right graph as compared to the left one.

The coherence spectra are plotted in Fig. 11(c). The maximal coherence corresponds to the shortest distance ($CE_\perp \approx 0.025$ rad) due to the shortest propagation time and vice versa—the signals "B" and "C" being separated at most by 0.1 rad show the lowest coherence. Note that in spite of the coherence level for *BC* combination is about 2% only [right graph **(c)**] the cross-phase shows the reliable spectrum from which the time delay Δt can be deduced. It evidences that the parasitic correlations in the system are very low.

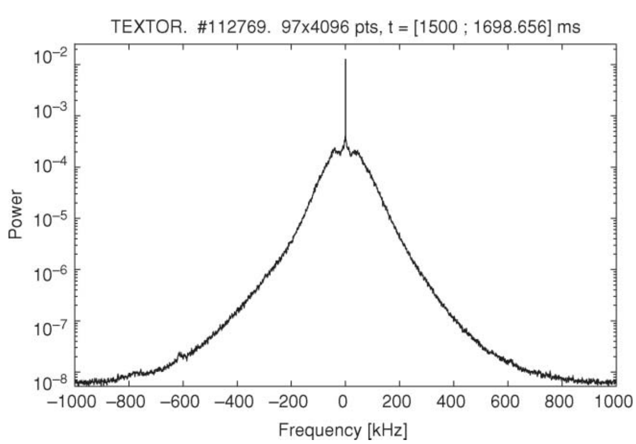

FIG. 9. Power spectrum of one of reflectometer channels measured in ohmic heated plasma. The dynamic range exceeds 60 dB.

B. Turbulence rotation

The examples of the turbulence rotation profile measured in different plasma scenarios are presented in Fig. 12(a). The rotation in the ion/electron diamagnetic drift (IDD/EDD) direction corresponds to positive/negative Ω values, respectively. The rotation of fluctuations in ohmic heated plasmas (without external momentum source) reveals the "rigid body" character: $\Omega(\rho) = \text{const}$. When NBI is being applied (even

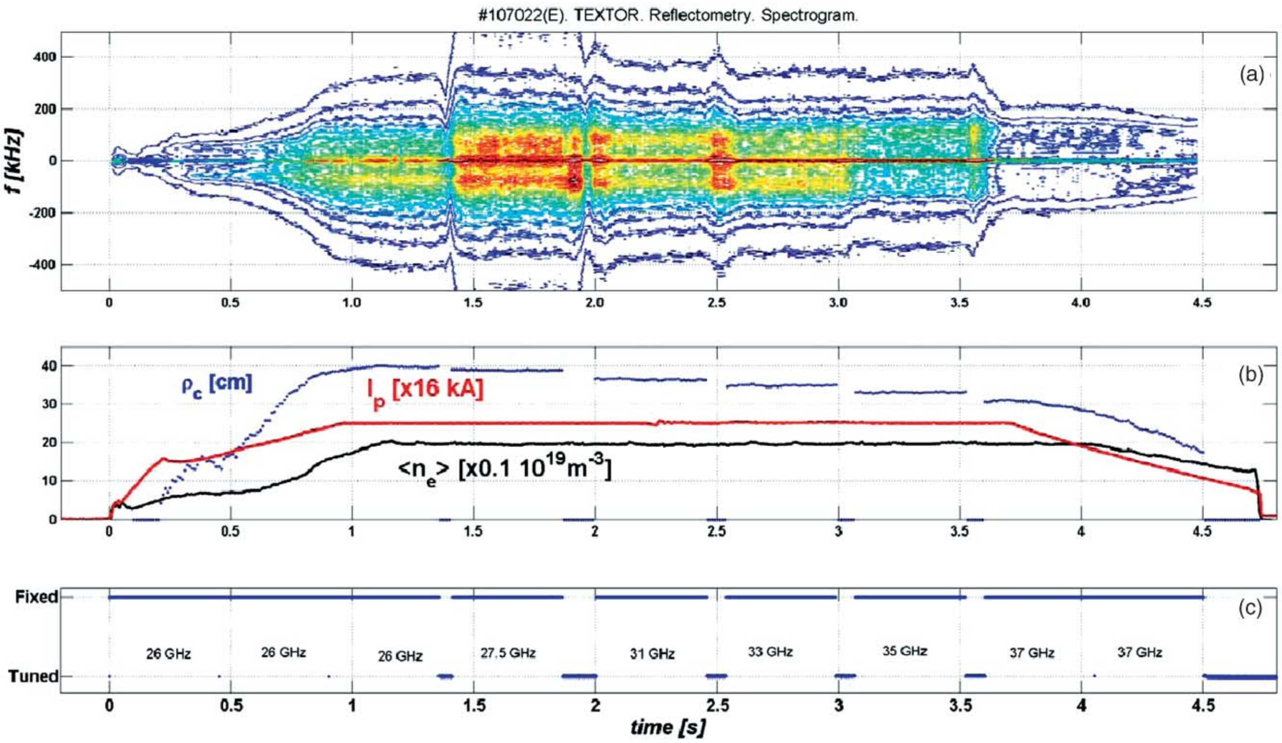

FIG. 10. (Color online) An example of reflectometer hopping operation with nine frequency steps for 4.5 s. (a) Fourier spectrogram. (b) Plasma electron density (n_e), current (I_p), and radius of the cutoff (ρ_c). (c) Operation frequency status "Fixed"/"Tuned."

of small power) it changes the central rotation of plasma column significantly. A co-I_p NBI for given helicity results in the reversal of intrinsic rotation of ohmic heated plasmas from EDD to IDD direction (compare crosses and squares on the graph). On the contrary, counter–I_p NBI adds to the ohmic rotation thus accelerating the plasma (compare crosses and triangles). At the same time, the turbulence rotation at the plasma edge is nearly insensitive to NBI, staying close to

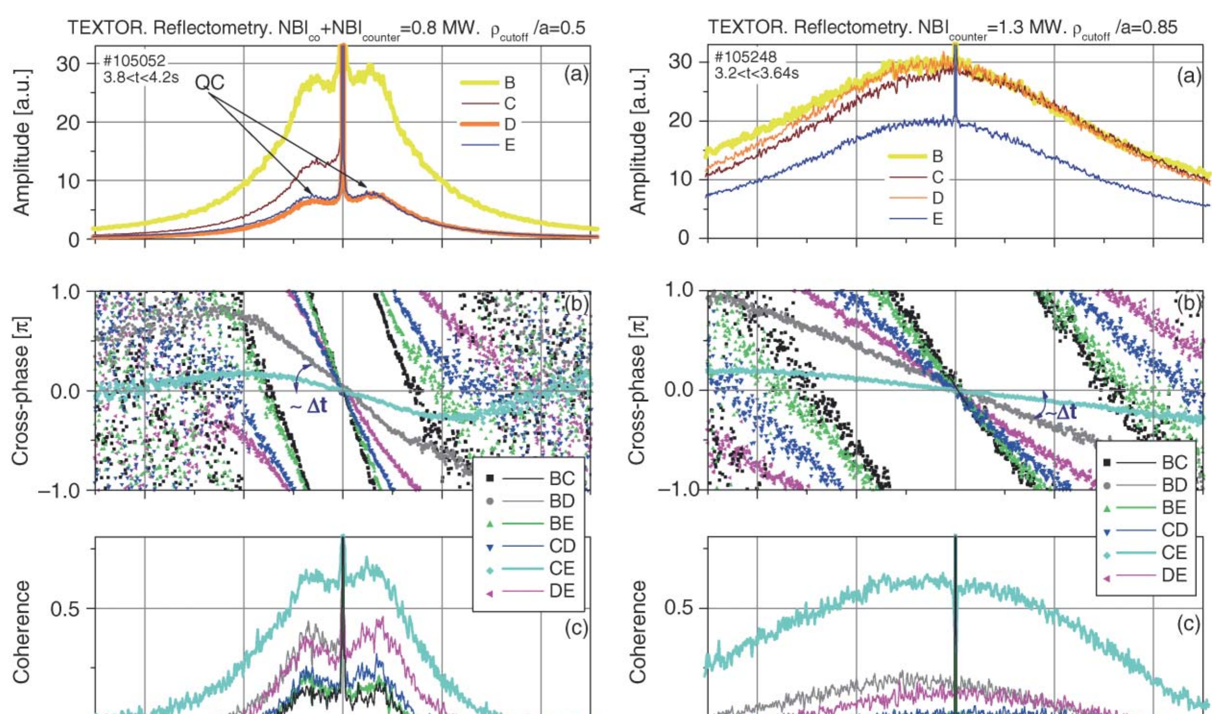

FIG. 11. (Color online) Turbulence spectral analysis for two NBI-heated plasmas: (left) balanced injection, $NBI_{co} = NBI_{counter} = 0.4$ MW; (right) unbalanced NBI-counter of 1.3 MW. (a) Amplitude, (b) cross-phase, and (c) coherence spectra for different antennae combinations.

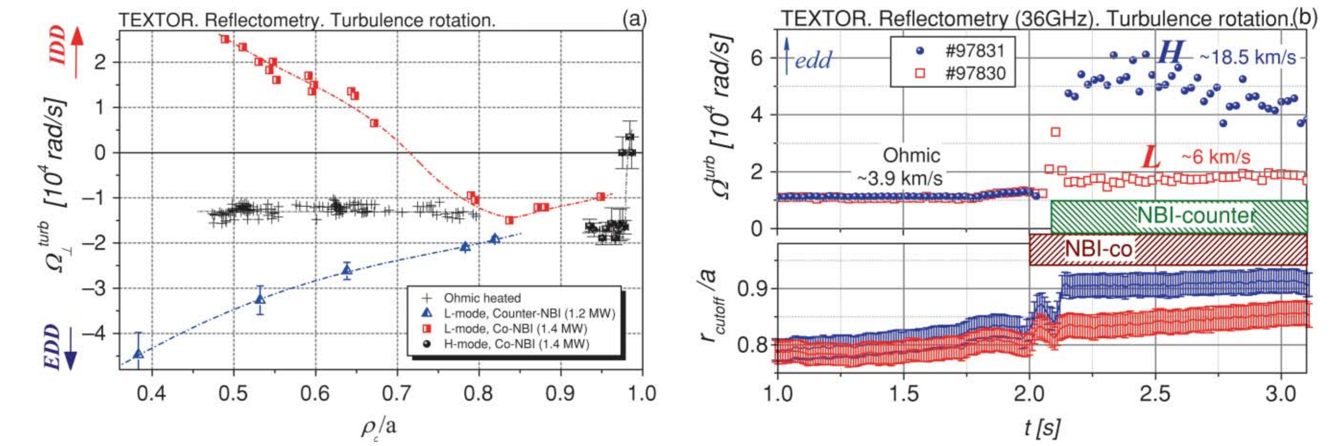

FIG. 12. (Color online) (a) Rotation data from CR for ohmic heated plasmas are shown by crosses. Rotation in plasmas with external momentum input, NBI-counter, and NBI-co, are displayed by triangles and squares, respectively. Rotation in H-mode near the pedestal is depicted by circles. (b) Rotation and cutoff position traces for shots with and without L–H transition (NBI-co & NBI-counter of 1.4 MW are used). (Ref. 14)

one in ohmic heated plasmas. An example of the turbulence rotation profile in H-mode plasmas characterized by sharp gradient near the pedestal is depicted by circles. L–H transition in plasmas heated with balanced NBI is found to be accompanied by a large change in absolute value of the turbulence rotation at the plasma edge, see $\Omega(t)$ traces in Fig. 12(b).[14] A clear rotation increase by ∼3 times in EDD direction at $t \approx 2.15$ s is associated with a decrease of radial electric field.

It is worth to note a restriction of the correlation method for velocity measurements. The measurements are possible if the turbulence decorrelation time is larger than, or the same order of magnitude as turbulence propagation time: $\tau_{dc} \gtrsim \Delta t$. When the turbulence rotation decreases so much that its propagation time prevails its decorrelation time, the correlation between reflectometer channels drops making the correlation measurements unfeasible (see a gap in data points shown by squares in Fig. 12(a) near a reverse point at $0.68 < \rho/a < 0.79$). Besides the measurements of the mean propagation velocity, its oscillating component can be also diagnosed. The velocity oscillations appear when the oscillating plasma flows, so called zonal flows and related geodesic acoustic mode (GAM), are developed.[15] With the use of CR we have measured both spectral and long-range correlation properties of GAM and proven its global nature.[16]

C. Turbulence decorrelation time

A set of distances between the detecting points (reflecting spots) along the turbulence propagation path allows to estimate both the correlation length and the decorrelation time (τ_{dc}) of the fluctuations. In Fig. 13 an example of the radial profile of τ_{dc} is presented for three different plasma states: L-mode, H-mode before edge localized mode (ELM) crash and H-mode after ELM crash.[14] One sees the difference is not only between L- and H-mode plasmas but also within an ELM cycle. The decorrelation time after ELM crash (recovery stage) is lower than before ELM crash (relaxation stage) that agrees with the turbulence level evolution on the ELM time scale.[17]

D. Phase Measurements

The phase measurements are very important for interpretation of reflectometry signals. The large-scale instabilities such as MHD modes and GAM contribute mostly in phase fluctuations of the probing wave. An example of reflectometer reconstructed phase when its probing wave is modulated by $m/n = 2/1$ MHD mode of ∼2 kHz is shown in Fig. 14. Here, in the lower part of graph the reconstructed reflectometer phase traces measured at two positions on the same density surface spaced poloidally and toroidally by $\sim 90^\circ$ and $\sim 113^\circ$, respectively are shown. The radius of reflection is close to the radial location of $m/n = 2/1$ MHD mode. For comparison, the signal from Mirnov Coil (MC) positioned close to the top antenna system is shown in the upper part of graph (gray line is of low-passed-filtered). The signals from MC and CR's top antenna being at close locations are antiphased because the "O" point of the magnetic island corresponds both to the maximum of MC signal and the maximal shift of the cutoff position outward that is a minimum of the probing wave phase.

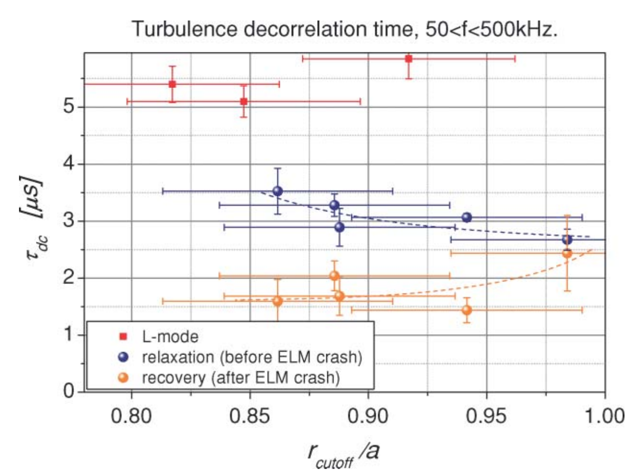

FIG. 13. (Color online) Turbulence decorrelation time, τ_{dc}. H-mode plasmas before and after ELM crash are compared with L-mode plasmas. (Ref. 14)

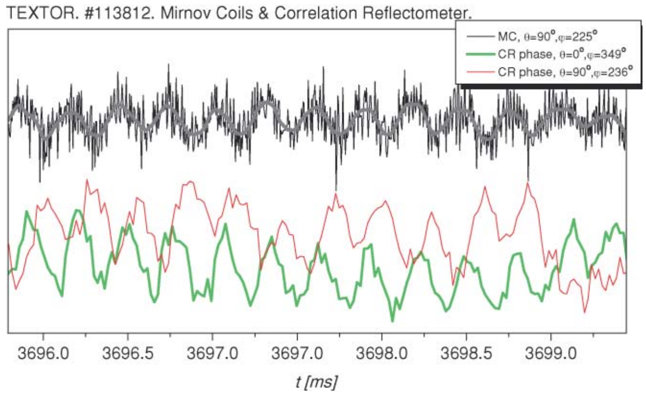

FIG. 14. (Color online) An example of direct phase measurements with CR when its probing wave is modulated by $m/n = 2/1$ MHD mode of $\sim$2 kHz. The reflectometer reconstructed phase measured at two positions on the same density surface as well as the signal of Mirnov Coil (MC) are shown in the lower and upper part of graph, respectively. The phase shift between signals is due to poloidal and toroidal separation.

A standard deviation of the probing wave phase, σ_ϕ, can be used for the estimation of the density fluctuation level.[4,13,18] In Fig. 15(a) an example of the mean phase and σ_φ versus time are presented by thin black and thick red/gray lines, respectively. The measurements are performed in ohmic heated plasma with a slow density scan, and the evolution of line averaged density ($\langle n_e \rangle$) and reflectometer cutoff (r_{cutoff}) are plotted in Fig. 15(b). The reflectometer operates in two steps: first at 26 GHz for $0 < t < 0.9$ s and after at 29 GHz for $1 < t < 8$ s. The density increases almost linearly for $1 < t < 4.3$ s and after is followed by the gas puff switch off and the diminishing of plasma current within $4.5 < t < 5.9$ s that serves a smooth decay of discharge accompanied by density decrease. A low turbulence level allows to reconstruct almost a full phase run of reflectometer which agrees well with $r_{\text{cutoff}}(t)$ history. The phase fluctuation level $\sigma_\varphi(t)$ increases when the cutoff moves out of the plasma center being consistent with σ_φ radial profile for ohmic heated plasmas.[13]

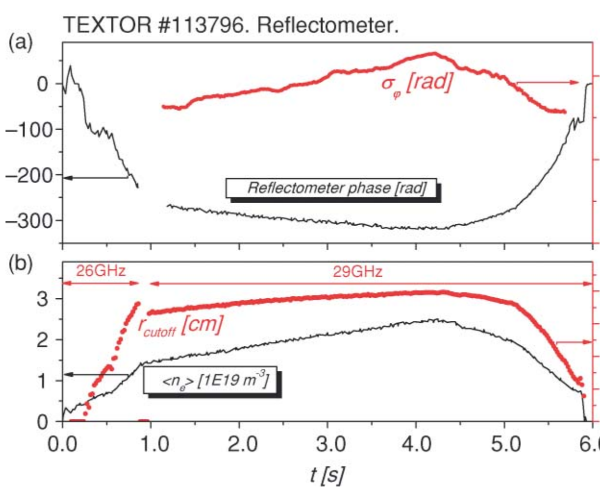

FIG. 15. (Color online) Reflectometer phase measurements in ohmic heated plasma with a slow density scan. (a) Mean phase of the probing wave as well as a phase standard deviation, σ_φ, are shown thin black and thick red/gray lines, respectively. (b) Reflectometer cutoff position and line averaged density are depicted with red/gray circles and thin black line, respectively.

VII. CONCLUSIONS

The low noise heterodyne hopping reflectometer system was developed for TEXTOR experiment. Being installed in 1998 it successfully operates more than 10 years providing the measurements of plasma density fluctuations. The use of low-noise, highly linear YIG sources which can be precisely tuned within a full K_α band of 26–37 GHz, allowed to design the reflectometer without frequency multiplication and power amplification. It enables a clean IF spectrum free from spurious and side-bands peaks. The resulted dynamic range of the system exceeds 60 dB. The cost for that, however, is relatively slow sweeping time ($\sim$10–100 ms) due to high inductive controlling windings used in the device. In spite of that and owing to the convenient interface software, the system can be programmed in the proper way to provide the hopping operation at desirable frequencies and in desirable time intervals during a plasma discharge. Thanks to the advanced multi-horn antenna systems the correlation properties as well as the propagation velocity measurements are possible in the wide range of plasmas. Note that in rare cases of very slow rotating plasmas (e.g., in the radial region of reversal of the velocity profile), when the turbulence decorrelation time becomes less than its propagation time the correlation measurements becomes unfeasible. Besides the ability to perform the correlation measurements, another advantage of the multiantenna registration is the increased reliability and decreased errors in the measurements of $\Omega_\perp^{\text{turb}}$ even in highly turbulent L-mode plasmas.

ACKNOWLEDGMENTS

We like to acknowledge Fedir Bereziuk (State Research Institute "ORION") for the upgrade of TEXTOR reflectometer and its inspection on site.

1A. Costley, P. Cripwell, and A. C. C. Sips, Rev. Sci. Instrum. **61**(10), 2823 (1990).
2T. L. Rhodes, R. J. Taylor, and W. A. Peebles, Rev. Sci. Instrum. **66**, 824 (1995).
3R. Nazikian and E. Mazzucato, Rev. Sci. Instrum. **66**(1), 392 (1995).
4E. Mazzucato, Rev. Sci. Instrum. **69**(6), 2201 (1998).
5S. Hacquin, L. Meneses, L. Cupido, N. Cruz, and L. Kokonchev, Rev. Sci. Instrum. **75**, 3834 (2004).
6K. Shinohara, R. Nazikian, T. Fujita, and R. Yoshino, Rev. Sci. Instrum. **70**(11), 4246 (1999).
7A. E. Costley, P. Cripwell, and G. Vayakis, JET Report JET–P(93)102, 1993.
8A. Y. Stepanov, V. N. Budnikov, E. Z. Gusakov, L. A. Esipov, E. R. Its, A. D. Piliya, V. V. Rozhdestvensky, and V. Yu. Shorikov, Fusion Eng. Des. **34–35**, 507 (1997).
9V. Vershkov, V. V. Dreval, and S. V. Soldatov, Rev. Sci. Instrum. **70**, 1700 (1999).
10G. D. Conway, G. Vayakis, J. A. Fessy, and D. V. Bartlett, Rev. Sci. Instrum. **70**(10), 3921 (1999).
11A. Krämer-Flecken, S. Soldatov, B. Vowinkel, and P. Müller, Rev. Sci. Instrum. **81**, 113502 (2010).
12S. Soldatov, A. Krämer-Flecken, and C. N. Klimov, Fusion Eng. Des. **84**, 6471 (2009).

[13] A. Krämer-Flecken, V. Dreval, S. Soldatov, A. Rogister, V. Vershkov, and TEXTOR Team, Nucl. Fusion **44**, 1143 (2004).
[14] S. Soldatov, A. Krämer-Flecken, B. Unterberg, and TEXTOR Team, Proceedings of the 33rd European Conference on Plasma Physics, Rome, 2006, Vol. 30I, paper P-2.164, http://epsppd.epfl.ch/Roma/pdf/P2_164.pdf.
[15] A. Krämer-Flecken, S. Soldatov, H. R. Koslowski, O. Zimmermann, and TEXTOR Team, Phys. Rev. Lett. **97**, 045006 (2006).
[16] A. Krämer-Flecken, S. Soldatov, D. Reiser, M. Kantor, and H. R. Koslowski, Plasma Phys. Controlled Fusion **51**, 015001 (2009).
[17] S. Soldatov, A. Krämer-Flecken, M. Kantor, B. Unterberg, Y. Sun, G. V. Oost, D. Reiter, and the TEXTOR Team, Plasma Phys. Controlled Fusion **52**, 085001 (2010).
[18] V. A. Vershkov, D. A. Shelukhin, S. V. Soldatov, A. O. Urazbaev, S. A. Grashin, L. G. Eliseev, A. V. Melnikov, and the T-10 team, Nucl. Fusion **45**, S203 (2005).